Effect of coarse aggregate size on non-uniform stress/strain and drying-induced microcracking in concrete

Gao, Peng; Chen, Yang; Huang, Haoliang; Qian, Zhiwei; Schlangen, Erik; Wei, Jiangxiong; Yu, Qijun

DOI
10.1016/j.compositesb.2021.108880

Publication date
2021

Document Version
Final published version

Published in
Composites Part B: Engineering

Citation (APA)
Gao, P., Chen, Y., Huang, H., Qian, Z., Schlangen, E., Wei, J., & Yu, Q. (2021). Effect of coarse aggregate size on non-uniform stress/strain and drying-induced microcracking in concrete. *Composites Part B: Engineering*, *216*, 1-18. Article 108880. https://doi.org/10.1016/j.compositesb.2021.108880

Composites Part B 216 (2021) 108880

Contents lists available at ScienceDirect

Composites Part B

journal homepage: www.elsevier.com/locate/compositesb

Effect of coarse aggregate size on non-uniform stress/strain and drying-induced microcracking in concrete

Peng Gao [a], Yang Chen [a,c], Haoliang Huang [a,b], Zhiwei Qian [d], Erik Schlangen [e], Jiangxiong Wei [a,b,*], Qijun Yu [a,b]

[a] School of Materials Science and Engineering, South China University of Technology, 510640, Guangzhou, China
[b] Guangdong Low Carbon Technologies Engineering Centre for Building Materials, 510640, Guangzhou, China
[c] Guangdong Provincial Academy of Building Research Group Co.Ltd, 510500, Guangzhou, China
[d] FEMRIS, The Hague, 2497, CJ, the Netherlands
[e] Microlab, Faculty of Civil Engineering and Geosciences, Delft University of Technology, 2628, CN, Delft, the Netherlands

ARTICLE INFO

Keywords:
Drying shrinkage
Microcracks
Tensile stress shell
Aggregate size
DIC
Lattice modelling

ABSTRACT

Non-uniform stresses, strains and microcracking of the concretes with three coarse aggregate sizes (5–10 mm, 10–16 mm, 16–20 mm) dried under 40% relative humidity (RH) for 60 days were quantified using digital image correlation and lattice fracture modelling. The influencing mechanism of coarse aggregate size on the drying-induced microcracking of concrete was clarified: (1) As the coarse aggregate size decreases, propagation paths of microcracking are increased, which increase the number of small microcracks and release the drying shrinkage force from mortar phase. (2) Tensile stress shells surrounding the coarse aggregates become thinner, thereby decreasing the area of large microcracks. As the coarse aggregate size decreased from 16-20 mm to 5–10 mm, the average thickness of tensile stress shells decreased from 2.13 mm to 1.09 mm at the beginning of drying, and the area of the microcracks >5 μm in width decreased from 796.6 mm^2/m^2 to 340.2 mm^2/m^2 at 60 days since drying.

1. Introduction

Drying shrinkage is a common issue of concrete structure [1–4]. Mortar phase and coarse aggregates are two main phases in concrete. The main components of the mortar phase consist of cement paste and fine aggregates. Being exposed to drying condition, the cement paste shrinks due to the moisture evaporation to environment, causing the shrinkage of the mortar phase. On the concrete scale, this shrinkage of the mortar phase is restrained by the coarse aggregates, which rises internal stresses in concrete. Once these internal stresses exceed the local strength in concrete, microcracking occurs and might lead to serious damage of concrete [5,6].

The drying-induced microcracking in concrete is influenced by many factors, such as the ambient relative humidity (RH) and temperature, the properties of binders, and the properties of aggregates. Because the aggregate size is an important parameter for concrete mix design, many studies concerned the drying-induced microcracking of the concretes with different aggregate sizes [5–9]. Bisschop and Van Mier [5] used the fluorescent epoxy impregnation method to observe the drying-induced microcracking of concrete. They found that the total length of microcracks increased with increasing the aggregate size. Also applying the fluorescent epoxy impregnation method, Wu et al. [6] observed that both the average width and total area of microcracks increased as the aggregate size increased. Numerical models are also attracting increasing interest in studying the drying-induced microcracking in concrete. By using a lattice approach, Grassl et al. [7] simulated the drying-induced microcracks in concrete and found that the concrete with larger aggregate size showed larger width of microcracks, while the microcracks' density was smaller. By using a hygro-mechanical model, Idiart et al. [8,9] simulated the drying-induced microcracking of concrete, and found that the concretes prepared with larger aggregates exhibited larger degrees of microcracking.

These studies suggested that the drying-induced microcracking in concrete could be reduced by optimizing the aggregate size. However, there remains a need for clarifying the mechanism behind the effect of aggregate size on the microcracking of concrete under drying condition. Goltermann [10,11] calculated the stress distribution in the concrete based on classical elasticity theories. The calculation illustrated that

* Corresponding author. School of Materials Science and Engineering, South China University of Technology, 510640, Guangzhou, China.
E-mail address: jxwei@scut.edu.cn (J. Wei).

https://doi.org/10.1016/j.compositesb.2021.108880
Received 11 December 2020; Received in revised form 4 April 2021; Accepted 5 April 2021
Available online 16 April 2021

Table 1
Mix proportions for mortar and concrete (kg/m^3).

Specimen	Cement	Water	Fine aggregates	Coarse aggregates		
				5–10 mm	10–16 mm	16–20 mm
Mortar	910	364	901	–	–	–
Concrete-S	554	222	541	1083		
Concrete-M	554	222	541		1083	
Concrete-L	554	222	541			1083

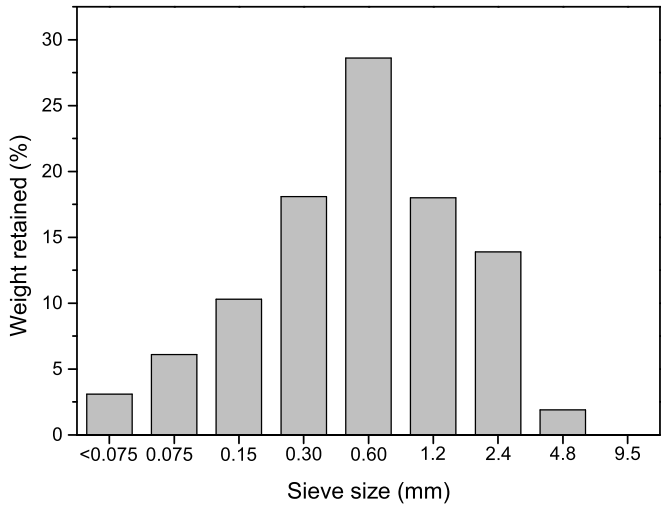

Fig. 1. Grading of fine aggregates (data is from Ref. [31]).

Table 2
Volume fractions of components for mortar and concrete.

Specimen	Cement	Water	Fine aggregates	Coarse aggregates		
				5–10 mm	10–16 mm	16–20 mm
Mortar	0.29	0.37	0.34	–	–	–
Concrete-S	0.17	0.22	0.20	0.41		
Concrete-M	0.17	0.22	0.20		0.41	
Concrete-L	0.17	0.22	0.20			0.41

tensile stress shells would form tangentially to the aggregate's boundary due to the restraining effect of aggregate on the matrix's shrinkage, and the tensile stress shells could cause the formation and propagation of microcracks. However, the value of the tensile stress was independent of the aggregate size. Similar result was found in the numerical study of Moon [12]. Hence, it could be inferred that other factors rather than the value of the tensile stress are more important to affect the drying-induced microcracking in the concretes with different aggregate sizes.

Because the shape and spatial distribution of aggregates are generally heterogeneous, the restraint of aggregates on the matrix's shrinkage will cause non-uniform deformations in concrete [13]. The mechanism of drying-induced microcracking could be better understood if the non-uniform stresses/strains in concrete can be captured [13].

As the developments in material measurement, the non-uniform strains in concrete were increasingly concerned. For example, Digital image correlation (DIC) was proposed to determine the non-uniform strains of materials by applying correlation algorithm to compare the photos of specimen before and after deformation [14–16]. Recently, DIC was increasingly applied to study the non-uniform properties of concretes [17–31]. Moelich et al. [25] used DIC in monitoring the plastic shrinkage of 3D-printed concrete. Lagier et al. [26] and Mauroux et al. [27] applied DIC to measure the drying-induced strains in the cement paste embedded with cylindrical aggregates, and those in coating mortar, respectively. By using DIC, Maruyama et al. [28–30] captured the drying-induced strains in concretes. Our recent study also utilized DIC to quantify the non-uniform strains in the concretes with different aggregate sizes and volume fractions [31]. These studies illustrate that DIC is attractive for investigating the non-uniform properties of concrete.

The measurement of non-uniform stresses in concrete seems to be more difficult compared with that of non-uniform strains probably due to the limitation on the stress sensor size. Alternatively, numerical models were preferred in obtaining the non-uniform stresses in concrete. Moon [12] applied a finite element method to obtain the drying-induced stresses in concrete. Schlangen et al. [32] simulated the stresses in concrete by using the lattice fracture model. Recently, we also used the lattice fracture model to analyse the interaction between stresses and microcracking in concrete as drying continues [33,34].

As mentioned previously, extensive studies have been carried out to directly illustrate the influence of aggregate size on the properties of drying-induced microcracks, such as density and width. However, the influence of aggregate size on the drying-induced non-uniform stresses/strains of concrete remains unclear.

In this study, the aggregate size's effect on the drying-induced non-uniform stresses of concrete was quantified, which was used to clarify the influencing mechanism of aggregate size on the drying-induced microcracking. The local strains and stresses of concrete were obtained by combining the DIC technique and the lattice fracture modelling. To analyse the reliability of the stresses obtained from the lattice fracture model, the comparison was carried out between the simulated drying-induced shrinkage and microcracks with those determined using DIC. Then, the relationships among aggregate size, stresses and dying-induced microcracks were established to analyse the drying-induced microcracking in the concretes with different aggregate sizes.

2. Experimental methods

2.1. Mix proportions

The C40 concretes were designed. Table 1 exhibits the component proportions of the concretes. Type I 42.5 cement was used as binder. The fine aggregates were produced by crushing large aggregates into sand-sized aggregate particles (fineness modulus = 2.8). Fig. 1 shows the particle size distribution of the fine aggregates determined by using square-mesh sieve. The crushed granite was classified as three sizes: 5–10 mm (Concrete-S), 10–16 mm (Concrete-M) and 16–20 mm (Concrete-L) also by using the square-mesh sieve. The weight ratio of water: cement: fine aggregates (W/C/F) was set approximate 0.4: 1: 1 in the concretes. Table 2 shows the volume fractions of components for mortar and concrete. The volume ratio of the coarse aggregates was close to 0.41 in the concretes. The properties of these components such as the chemical composition of the cement, and the silt content of the coarse aggregates can be found in Ref. [31]. The mortar was prepared using the same ratio of W/C/F as the concretes, because its bulk drying shrinkage was applied in the lattice fracture model as input. According to the method mentioned in our recent studies [33,34], the concretes and mortar were cast into the 100 × 100 × 100 mm^3 specimens. After demoulding, the specimens were cured in the saturated calcium hydroxide solution up to 28 days (temperature = 23 °C).

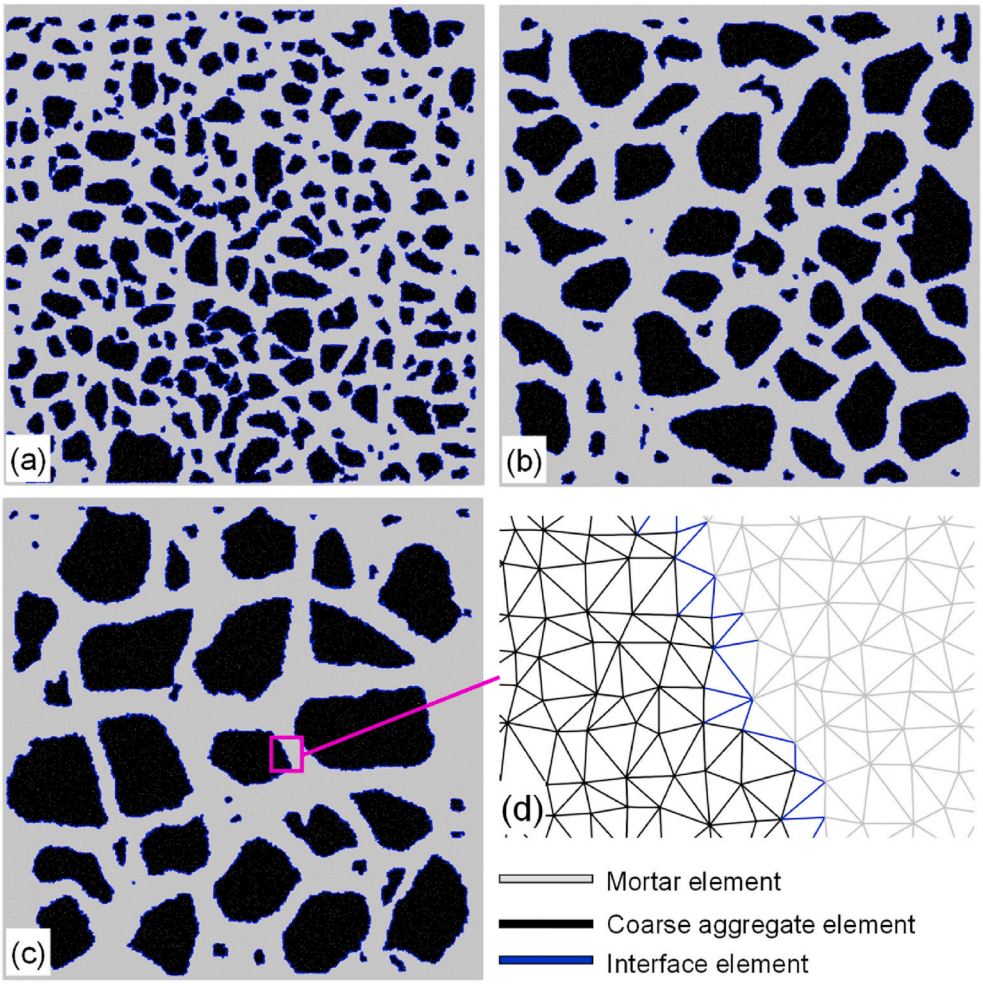

Fig. 2. Delaunay triangulation lattice meshes of Concrete-S (a), Concrete-M (b) and Concrete-L (c): the fractions of coarse aggregate nodes in (a), (b) and (c) were 0.37, 0.41, and 0.42, respectively. (d) zooms in the mesh.

2.2. DIC measurement

Due to moisture gradient, differential drying shrinkage might occur in concrete, which could also cause microcracking in concrete [35]. For the purpose of reducing the moisture gradient through the thickness, the concrete and mortar specimens were cut as slices (thickness = 10 mm) with a cutting machine. The cutting speed was set as 200 r/min to ensure the surface of concrete slice was smooth and no significant cracks were formed [34] (see an example in Appendix A). The central slices of concrete were used in the DIC test, as the gravity probably cause the loose and concentrated spatial distributions of coarse aggregates on the top and bottom of concrete, respectively [34]. The slices' surfaces for the DIC measurement were sprayed with stochastic speckle patterns. After that, the slices were dried in an isothermal chamber with temperature = 20 °C. Due to global warming, the extreme low RH conditions occur in many cities. For example, the cities such as Marrakech, Madird and Phonexis showed RH much smaller than 50% in the summer 2016 [35]. The extreme low RH conditions also occur in the northwest Chinese cities such as Ningxia and Yulin. In the current study, the RH of the isothermal chamber was set as 40% to concern the microcracking of concrete under the extreme low RH conditions. At 0, 1, 3, 7, 11, 28, 60 days since drying, the specimens were taken from the isothermal chamber for the DIC measurement (displacement accuracy = 5 μm [31]). After the DIC measurement, the specimens were continually dried in the isothermal chamber. Then, several subsets were assigned on the slice's surface by using the DIC software. The subsets' displacements, determined from the correlation of DIC images, were used to calculate the subsets' strains [31]. After that, the bulk drying shrinkage of slice ($\varepsilon_{ave,bulk}$) was calculated by considering the displacements of the subsets on the edges [34]. As reported in reported in Ref. [35], the surface and 10 mm depth in concrete could show 5% RH gradient. In the present study, both the top and bottom surfaces of concrete slices were dried in the isothermal chamber. Hence the moisture gradient through the concrete slice was probably smaller than 5% RH. However, this moisture gradient should be considered if the internal microcracking and damage of concrete are concerned.

2.3. Mechanical properties

The compressive strength of the specimens (mortar and concrete, $100 \times 100 \times 100$ mm^3) at 28 days since curing was measured by using the compression test following GB T50081-2002 [36].

3. Modelling methods

Generally, discretised lattice elements are used to represent the materials' structure in the lattice fracture modelling [37,38]. The lattice analysis consists of a sequence of linear analysis steps. At each analysis step, the lattice analysis is similar to the standard finite element method. The element that with highest stress/strength ratio, called critical element, is removed from the system in the lattice analysis [39]. Hence, the lattice analysis shows the potential to deal with the non-linear

Table 3
Mechanical properties of lattice elements in concrete [33,34,41].

	Elastic modulus (GPa)	Compressive strength (MPa)	Calculated tensile strength (MPa)
Coarse aggregate elements	80.0	90.0	9.0
Mortar elements	20.5	42.0	4.2
Interface elements	15.0	25.0	2.5

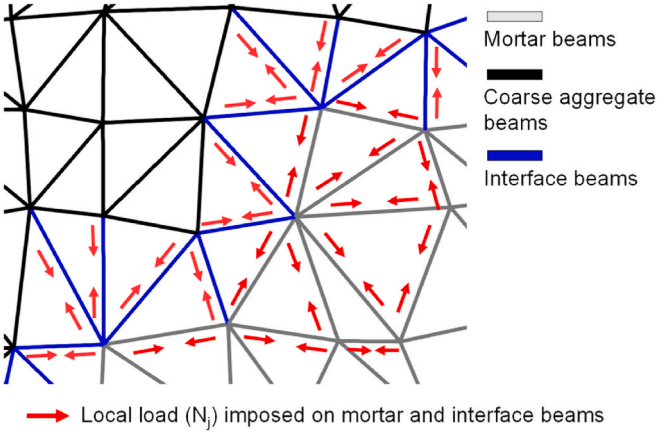

Fig. 3. Method for imposing drying-induced force on mortar and interface elements in lattice fracture modelling.

behaviours of materials. In addition, the lattice fracture modelling has the advantage in computing time and memory room [38,39]. Further, the lattice fracture model has been confirmed as attractive for modelling the fracture behaviours of cement-based materials [33,34,37–45]. The current study used a lattice fracture modelling program (GLAK) from the Delft University of Technology [38–40]. The modelling process was detailed as follows.

3.1. Lattice mesh

The concrete was simulated to consist of mortar, coarse aggregates, and the interface between mortar and coarse aggregates. A binary digital image processing was used to distinguish the coarse aggregates and mortar phase from the DIC image [33,34]. After that, the lattice mesh was established as follows.

(1) Randomness

Generally, the mesh size will influence the calculation results of lattice fracture model. For example, the morphological properties of coarse aggregates such as angularity will gradually lose with increasing the mesh size. On the other hand, the computing efficiency of lattice fracture model will significantly decrease as the mesh size decreases, because more lattice elements will be generated. By considering the morphology of coarse aggregates and the computing efficiency, the current study set the mesh size as 0.4×0.4 mm^2/grid. Then, the digital image of concrete was discretised into 250×250 square grids, followed by assigning a sub-cell in the grid's centre. In each sub-sell, a lattice node was randomly placed and defined as mortar or coarse aggregate node depending on the major component of the grid [33,34]. After that, the size ratio of sub-cell to grid was applied to adjust the randomness of lattice mesh [38–41]. This size ratio was set as 0.5 in the current study.

(2) Shape

Triangulation mesh can be used to simulate the deformations in cement-based materials [41]. This type of mesh was also applied in the current study by connecting the nodes as lattice elements based on the Delaunay triangulation method [41,46]. Then, three types of lattice elements were defined: mortar element connecting two mortar nodes, coarse aggregate element connecting two coarse aggregate nodes, and interface element connecting mortar and coarse aggregate nodes. Notably, Bisschop and Van Mier [5] found that the aggregates with size smaller than 1 mm showed very small restraining effect on the microcracking. Similar results were reported by Idiart et al. [8]. Hence, the current study did not involve the restraining effect of fine aggregates, and considered the fine aggregates and cement paste as one element phase. Fig. 2a, b and c show the established Delaunay triangulation lattice meshes for Concrete-S, Concrete-M and Concrete-L, respectively. Generally, the aggregate volume is also an important factor to impact the drying-induced microcracking of concrete. Grassl et al. [7] indicated that the microcracks' width increased as the aggregate volume increased. Since the current study focused on the aggregate size's effect on the drying-induced microcracking, we attempted to control the coarse aggregates' volume fractions of the concrete slice in a constant value. However, the coarse aggregates' volume fractions of concrete slices were slightly different. For the Concrete-S, Concrete-M, and Concrete-L shown in Fig. 2, the coarse aggregates' volume fractions were 0.37, 0.41, and 0.42, respectively. This difference was probably due to the variation of coarse aggregates' spatial distribution. In addition, the surface area of coarse aggregates might be digitalized as mortar phase in the binary digital image processing because the colour of surface area is close to that of mortar phase [33,34]. Since Concrete-S contained more surface area of coarse aggregates, the coarse aggregates' volume fraction might be underestimated in the binary digital image processing. Notably, the absolute volume fraction difference of coarse aggregates was smaller than 0.05. This volume fraction difference might be considered when analysing the results of the DIC measurement and the lattice fracture modelling.

(3) Mechanical properties

Based on the compression test described in section 2.3, the mortar, Concrete-S, Concrete-M and Concrete-L showed the compressive strength of 42.0 ± 0.7 MPa, 51.4 ± 0.7 MPa, 53.6 ± 0.4 MPa and 47.0 ± 0.4 MPa respectively. As shown in Table 3, the mechanical properties of lattice elements were mainly from literature [33,34,41]. The Rankine failure criterion was used as the fracture law of lattice elements, wherein the comparative stresses in lattice elements were required smaller than the strengths of lattice elements [39]. Notably, the interface elements' length was around 0.4 mm. This length was much larger than the size of the ITZ (normally approximate 30 μm [47]). However, by adjusting the mechanical properties of interface elements, the impact of the ITZ on the performance of concrete can be considered in the lattice fracture modelling [41]. Qian et al. [39,40] calculated the harmonic average of the coarse aggregates and mortar elements' elastic modulus as the interface element's elastic modulus, and set the minimum value of the coarse aggregates and mortar elements' tensile strength as the interface element's tensile strength. However, they did not calibrate the calculated mechanical properties of interface elements. Luković et al. [41] calibrated the mechanical properties of interface elements to make sure that the substrate showed similar strength as the repair materials. Recently, we [33,34] used the mechanical properties of interface elements of Luković et al. [41] in the lattice fracture modelling, and found that the simulated non-uniform deformations were consistent with the DIC observations. Hence, theses mechanical properties of interface elements were also used in the current study.

3.2. Drying-induced force imposed on lattice mesh

Under drying conditions, a local force will rise in concrete due to the

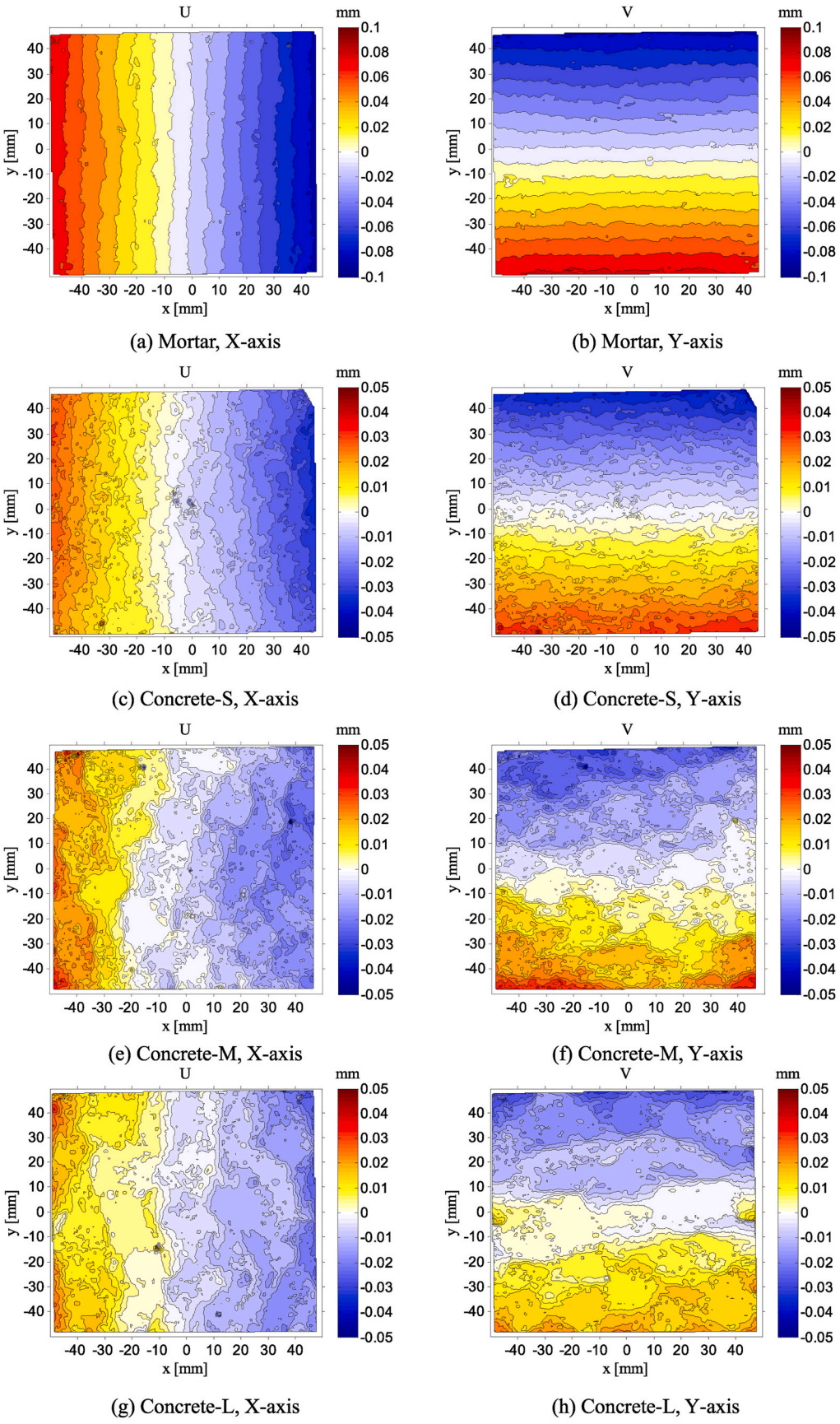

Fig. 4. Measured displacement fields of mortar and concrete slices under drying for 60 days: (a), (c), (e) and (g) are along X-axis; (b), (d), (f) and (h) are along Y-axis.

Table 4
Drying-induced forces imposed on the mortar and interface elements.

Time since drying (days)	Bulk shrinkage of mortar slice $\varepsilon_{m,bulk}$ (μm/m)	Force imposed on mortar and interface elements N_{sh} (kN)
1	574	1.55×10^{-3}
3	892	2.41×10^{-3}
7	1088	2.94×10^{-3}
11	1197	3.24×10^{-3}
21	1412	3.82×10^{-3}
28	1444	3.90×10^{-3}
60	1627	4.40×10^{-3}

shrinkage of the mortar phase. This drying-induced force (N_{sh}) can be obtained by considering the drying shrinkage (ε_m) and elastic modulus (E_m) of the mortar phase (see Eq. (1) [41]). The ε_m of the mortar phase in the concrete slice was considered as the bulk drying shrinkage of the mortar slice ($\varepsilon_{m,bulk}$), which was quantified using the DIC technique [33,34,41].

$$N_{sh} = \varepsilon_m E_m A \tag{1}$$

where A represents the cross-section area of element. $\varepsilon_m E_m$ represents the imposed local stress. In this study, A and E_m were set as 0.132 mm^2 and 20.5 GPa, respectively.

N_{sh} was loaded on the mortar elements according to the iteration algorithm in our previous studies [33,34]. First, a small force (N_j) was loaded on mortar elements at a step j (Fig. 3). Due to the restraining of other elements in the lattice mesh on this force, tensile stresses would rose in some elements. Then, GLAK would calculate the stress in each element, and search the element with the highest ratio of tensile stress to tensile strength, followed by increasing N_j until the element was broken. This process iterated until N_j increased to N_{sh}. At each step, GLAK would output the coordinates of each node and the residual stress in each

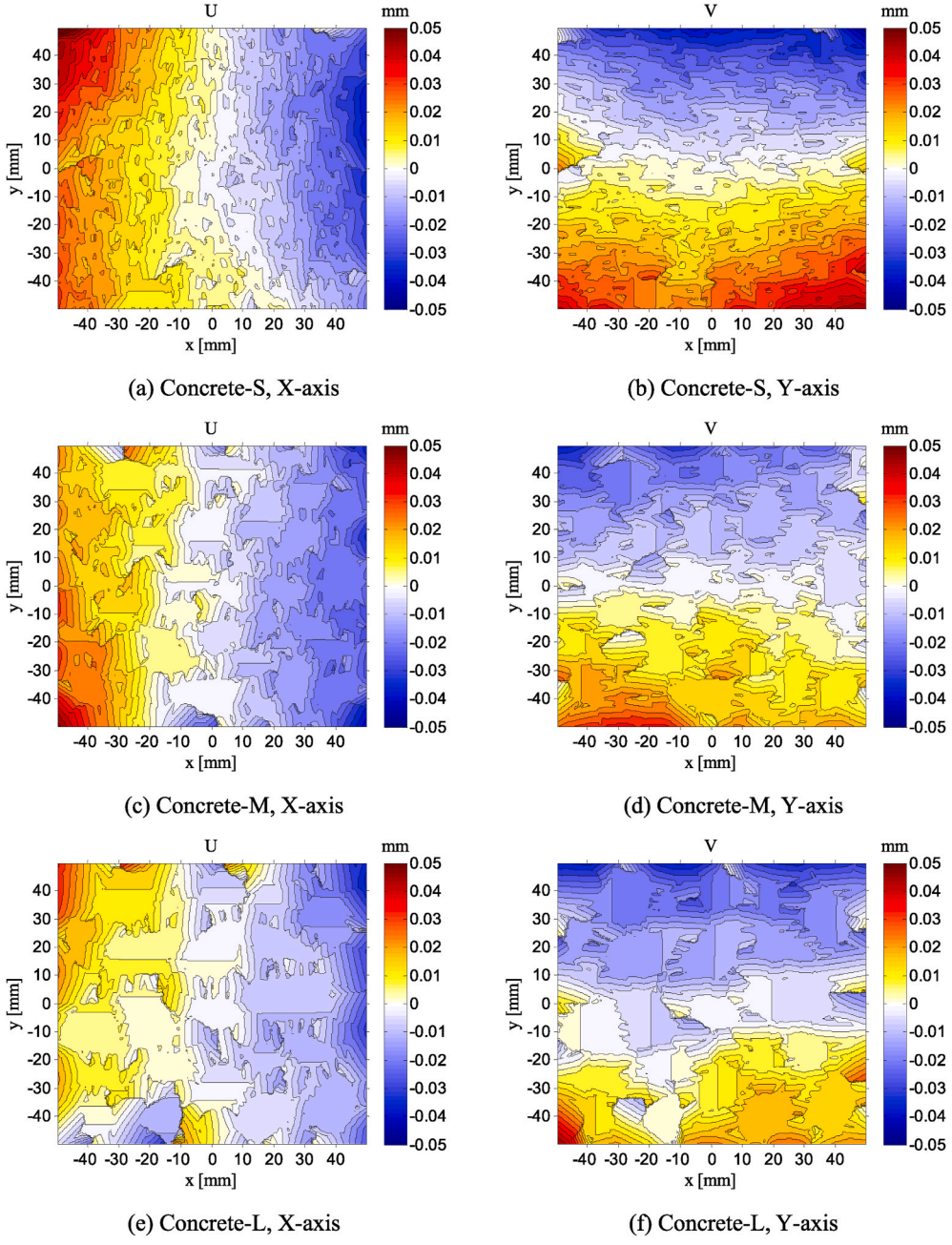

Fig. 5. Simulated displacement fields of concrete specimens under drying for 60 days: (a), (c) and (e) are along X-axis; (b), (d) and (f) are along Y-axis.

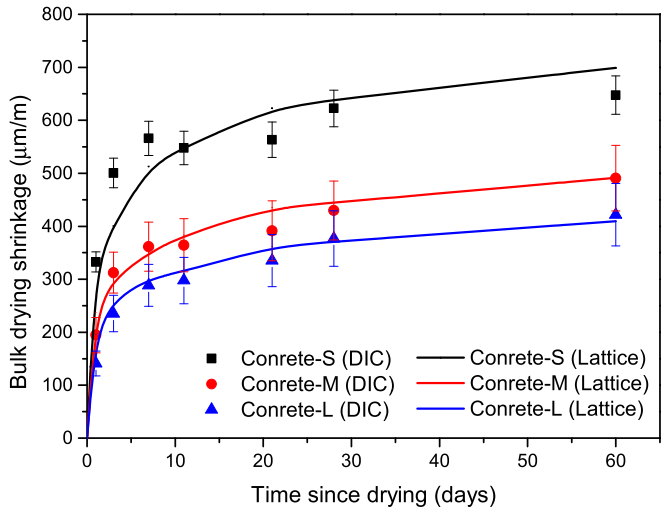

Fig. 6. Comparison between measured (DIC) and simulated (Lattice) bulk drying shrinkage of concretes with different coarse aggregate sizes under drying up to 60 days.

element.

Notably, the ITZ also affects the drying shrinkage of the concretes with different aggregate sizes [29], which should be considered in modelling the drying shrinkage of concrete. Maruyama and Sugie [29] proposed a constitutive law of element containing ITZ to simulate the drying shrinkage of concretes with different aggregate size. In the current study, N_{sh} was imposed on the interface elements to deal with the effect of ITZ on the drying shrinkage of concrete.

3.3. Boundary conditions

Generally, some nodes of the lattice mesh should be set as unmovable to avoid the floating of the lattice mesh in the lattice fracture modelling process. As observed by using the DIC (see section 4), the deformations of concrete slice were towards the centre. To compare with the DIC observation, the node in the lattice mesh centre were set as unmovable. Further, the coarse aggregate elements were assumed as unbreakable because the granite coarse aggregates used in this study have much larger strength than the ITZ and mortar.

3.4. Microcrack area and width

A broken lattice element was considered as a microcrack [33,34]. The width of microcracks was calculated using Eq. (2).

$$w_{i,j} = l'_{i,j} - l^0_i + \tag{2}$$

where l^0_i represents the distance of nodes before deformation, $l'_{i,j}$ represents the distance of nodes at modelling step j. $l'_{i,j} - l^0_i +$ is the positive part operator for $l'_{i,j} - l^0_i$, if $l'_{i,j} - l^0_i$ is negative, $l'_{i,j} - l^0_i +$ is calculated as zero.

The microcracks' total area of concrete was calculated following Eq. (3) [34].

$$A_{Crack,j} = \frac{\sum_i (w_{i,j} \times l_c)}{A_{Conrete}} \times 10^3 \tag{3}$$

where $A_{Crack,j}$ represents the microcracks' area per unit concrete's area (mm^2/m^2), l_c represents the cross length of lattice element (this value was set as 0.4 mm) and $A_{Conrete}$ represents the area of concrete slice (100 × 100 mm^2).

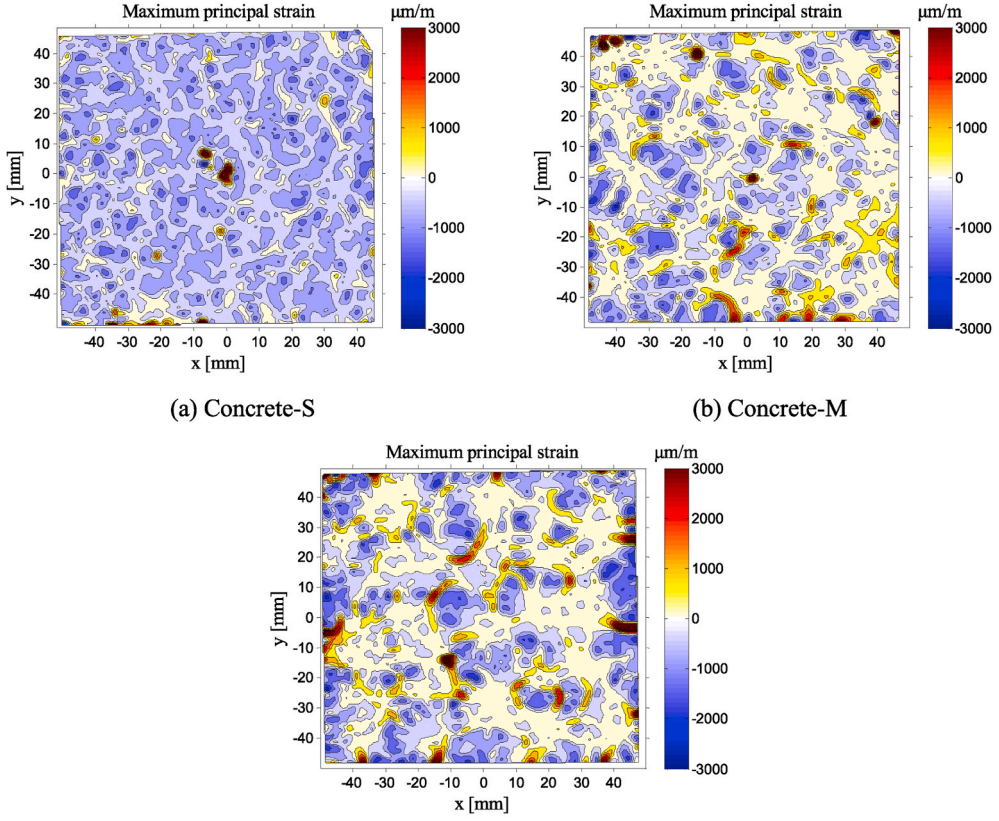

Fig. 7. Maximum principal strains (ε_{max}) in the concrete slices with different coarse aggregate sizes captured using DIC (60 days since drying).

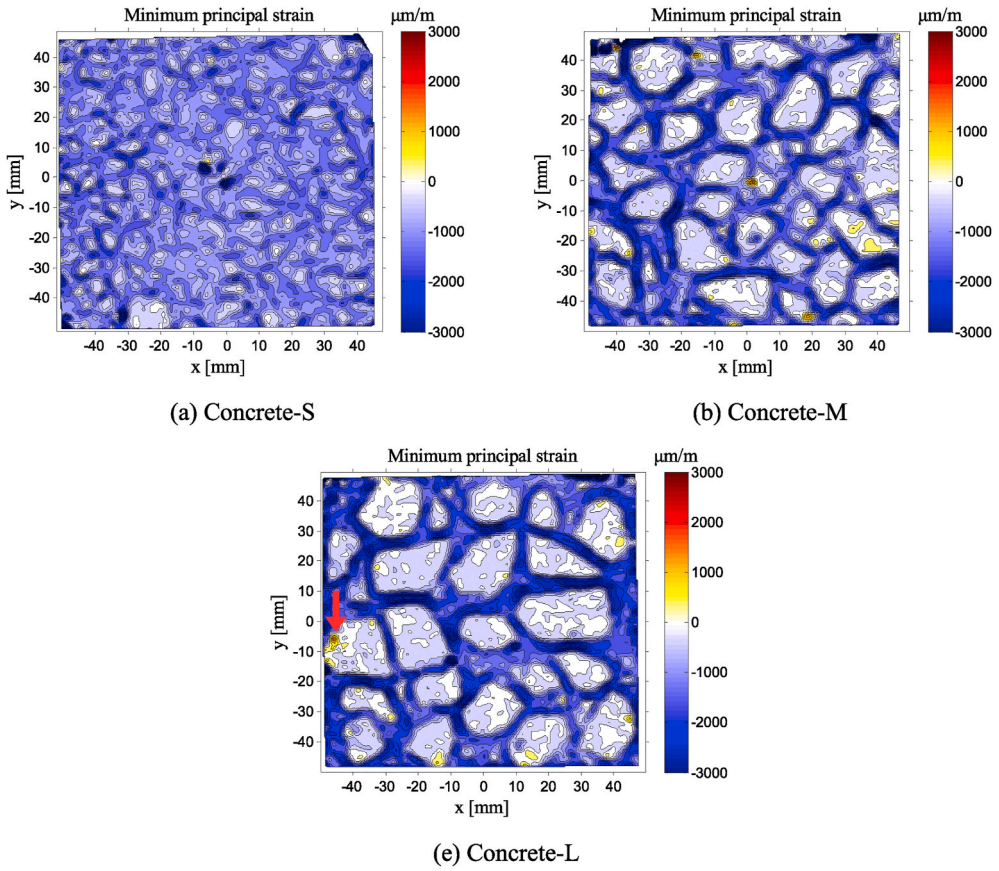

Fig. 8. Minimum principal strains (ε_{min}) of the concrete slices with different coarse aggregate sizes captured using DIC (60 days since drying).

3.5. Creep influence

Cement-based materials normally show viscoelastic characteristics [48]. Bažant and Jirásek [49] summarized that the rate of nanoscale bond fractures in C–S–H gel will occur as the formation of drying-induced stresses, thereby causing the drying creep in cement-based materials. In the present study, the DIC was applied to determine the total drying shrinkage of mortar slice ($\varepsilon_{m,bulk}$). By using Eq. (1), the drying-induced local force (N_{sh}) imposed on the mortar elements was calculated from the bulk drying shrinkage of mortar slice ($\varepsilon_{m,bulk}$). As indicated by Grasley et al. [50], $\varepsilon_{m,bulk}$ consists of true free shrinkage (ε_{sh}), drying creep (ε_{cr}) and remaining strain required for strain compatibility (ε_{el}). According to the data reported in Ref. [49], the drying creep can account for 30% of the total drying shrinkage of concrete at 100 days since drying. In the current study, the impact of drying creep (ε_{cr}) on the deformations of concrete was taken into account by applying Eq. (1) to calculate N_{sh}. However, the restraining of coarse aggregates and the formation of microcracks might redistribute the local stresses in concrete, which could change the drying creep in concrete. Further work should deal with this effect on the drying shrinkage of concrete.

4. Results and discussions

4.1. Deformations of mortar and concrete

Fig. 4 displays the displacement fields of the mortar and concrete specimens along the X- and Y-axis (determined by using the DIC). The red and blue show the displacements towards the positive and negative of axis, respectively. According to in Fig. 4c–h, the displacement fields in the concrete slices became non-uniform as the coarse aggregate size increased. This is mainly caused by the restraining of coarse aggregates on the drying shrinkage of mortar phase.

According to section 3.2, the bulk drying shrinkage of the mortar slice ($\varepsilon_{m,bulk}$) (determined using DIC) was used to calculate the drying-induced force imposed on the mortar and interface elements (N_{sh}). Table 4 shows the obtained N_{sh} at different drying times.

Fig. 5 displays the displacement fields of the concrete slices obtained using the lattice fracture model. The simulated displacement fields in the concrete slices became more heterogenous as the coarse aggregate size increased, which is consistent with the DIC observations.

Fig. 6 exhibits the simulated bulk drying shrinkage of concrete slices compared with experiment. At 60 days since drying, the bulk drying shrinkage of Concrete-S, Concrete-M and Concrete-L increased to 622 μm/m, 463 μm/m, and 403 μm/m, respectively, which are slightly smaller than the DIC data. This is probably because that the drying creep was not yet fully dealt with in the simulation. In addition, the bulk drying shrinkage of concrete slices decreased with increasing the size of coarse aggregate. This trend is in good agreement with the observations from literature, such as Maruyama and Sugie [29]. The main reason is that the shrinkage of interface elements is relatively large due to the low elastic modulus of interface elements, and more interface elements will exist in the concrete with constant coarse aggregate volume as the coarse aggregate size decreases.

4.2. Damage and microcracks in concrete

Fig. 7 shows the maximum principal strains (ε_{max}) in the concrete slices determined using DIC. The ε_{max} of the concrete slices were non-uniform, including tensile strains (positive) and compressive strains (negative). Concrete-M and Concrete-L show more areas with large tensile strains (orange and red).

As can be seen from Fig. 8, the ε_{min} of the concrete slices also include tensile strains (positive) and compressive strains (negative). Further, the

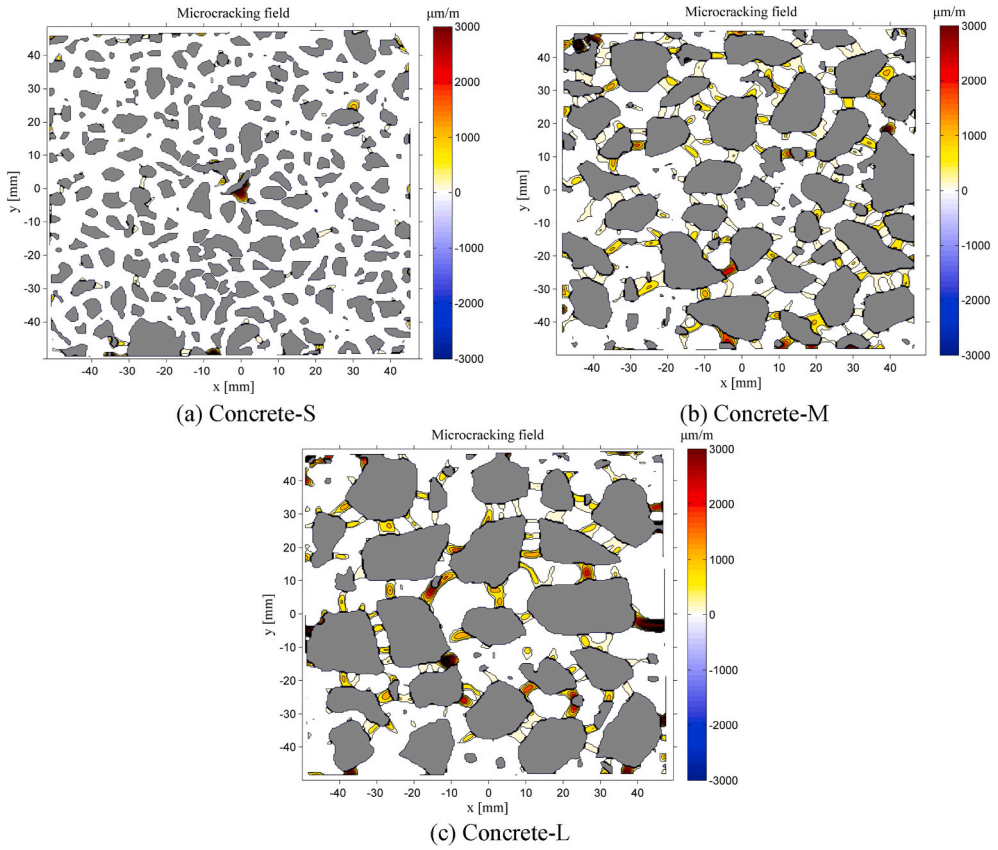

Fig. 9. Damage patterns in concrete slices under drying for 60 days determined using DIC. Grey represents coarse aggregates. Colour represents damage patterns. (For interpretation of the references to colour in this figure legend, the reader is referred to the Web version of this article.)

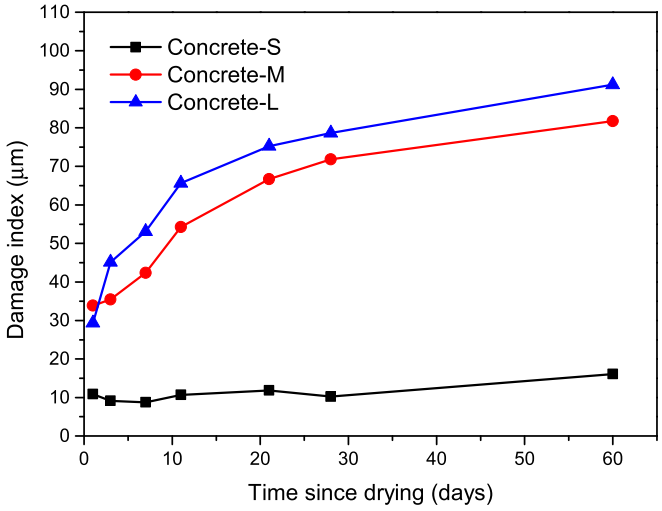

Fig. 10. Damage index ($D_{\widetilde{\varepsilon},m\&i}$) of concrete slices with different coarse aggregate sizes under drying up to 60 days.

patterns of $\varepsilon_{\min}$ could be used to identify the distribution of coarse aggregates, because the tensile strains in coarse aggregates were relatively small (white and light blue). Notably, some tensile strains can be found in coarse aggregates (red and orange, e.g. the area indicated by the arrow in Fig. 8c). The formation mechanism of these tensile strains in the coarse aggregates has been clarified in a recent study by our group [33]: With ongoing drying, the mortar shell that surrounds the coarse aggregates will be broken due to the formation of microcracks. Hence, the compressive stress imposed on the coarse aggregates will be released. In addition, due to the shrinkage of the mortar near the microcracks, a shear stress along the interface will be exerted. As a result, tensile strains could occur in the coarse aggregates.

Recently, identification of the damage patterns in concrete from non-uniform strains is increasingly concerned [26,27,34], because the non-uniform strains can be efficiently measured by the technique such as DIC. Several decades ago, Mazars [51] proposed the equivalent tensile strain ($\widetilde{\varepsilon}$) concept by combining $\varepsilon_{\max}$ and $\varepsilon_{\min}$ (see Eq. (4)), and indicated that the damage in concrete will occur if the value of $\widetilde{\varepsilon}$ is larger than the local threshold tensile strength (K_0) in concrete. Later, this concept was used by Lagier et al. [26], Mauroux et al. [27], and our recent study [34] to determine the patterns of drying-induced damage of concrete.

$$\widetilde{\varepsilon} = \sqrt{\varepsilon_{\max_+}^2 + \varepsilon_{\min_+}^2} \tag{4}$$

where $\widetilde{\varepsilon}$ represents the equivalent strain, and ε_+ represents the positive part operator for $\varepsilon_{\max}$ and $\varepsilon_{\min}$.

In the current study, the concept of $\widetilde{\varepsilon}$ was also considered to capture the drying-induced damage's patterns of the concretes with different coarse aggregate sizes. Because the interface and mortar phases showed much smaller strength than the coarse aggregates, the drying-induced damage was easy to form in the interface and mortar phases. Hence, this study focused on the drying-induced damage in the interface and mortar phases. The damage patterns were identified as follows: At first, the distributions of the mortar and interface phases were obtained by removing the coarse aggregates. Then, $\widetilde{\varepsilon}$ in the mortar and interface phases was calculated according to Eq. (4) and used to identify the patterns of $\widetilde{\varepsilon} > K_0$. According to the method of Lagier et al. [26], the K_0 was calculated from the tensile strength ($f_{t,mortar}$) and elastic modulus (E_{mortar}) of mortar, viz., $K_0 = f_{t,mortar}/E_{mortar}$. By using the mechanical properties of mortar shown in Table 3, the K_0 was calculated as 204

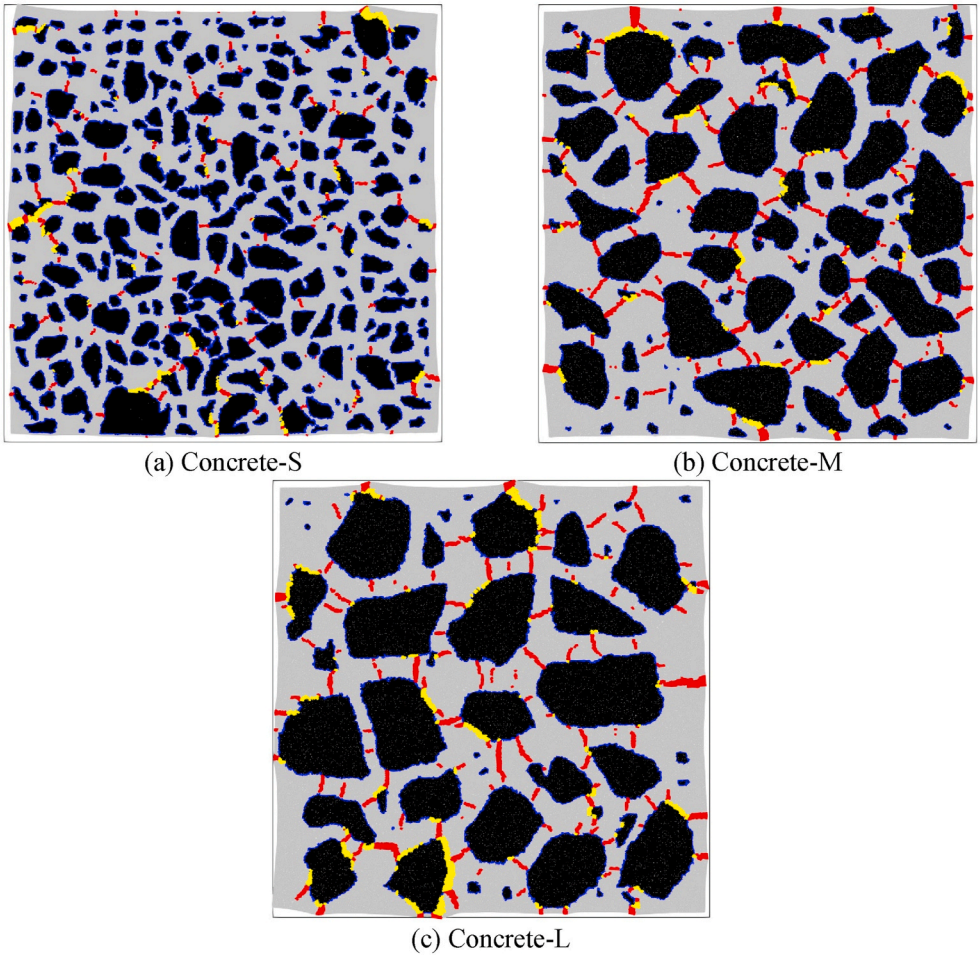

Fig. 11. Patterns of >5 μm microcracks in concrete slices under drying for 60 days (obtained using lattice fracture model): grey is mortar, blue is interface, black is concrete, red is microcrack in mortar, yellow is microcrack in interface. Deformations and microcracks are magnified 50 times. (For interpretation of the references to colour in this figure legend, the reader is referred to the Web version of this article.)

μm/m.

Fig. 9a, b and c show the identified damage patterns in Concrete-S, Concrete-M, and Concrete-L, respectively. In Concrete-M and Concrete-L, the damage patterns were significant and radially connected coarse aggregates. Notably, the damage caused by the microcracks <5 μm in width might not be identified because the DIC set-up used in current study shows the displacement accuracy of 5 μm.

In the studies of Maruyama et al. [28,29], a damage index (D_ε) was used to evaluate the degree of microcracking in concrete (see Eq. (5)). This D_ε showed good correlation with the bulk drying shrinkage of concrete [28]. However, the D_ε might overestimate the damage in concrete because the threshold tensile strain (K_0) was set as 0 μm/m. Our recent study [34] proposed a new damage index ($D_{\tilde{\varepsilon}}$) by combining the equivalent tensile strain concept and the research of Maruyama et al. [28,29]. We found that the $D_{\tilde{\varepsilon}}$ increases linearly with the microcracks' area obtained using the lattice fracture model. Since the current study concerned the microcracks in mortar and interface, we modified the $D_{\tilde{\varepsilon}}$ as $D_{\tilde{\varepsilon},m\&i}$ by considering the area of $\tilde{\varepsilon}_i > K_0$ in the subset of mortar or interface (see Eq. (6)).

$$D_\varepsilon = \frac{\sum_i \left(\varepsilon_{\max,i} \cdot A_i \middle| \varepsilon_{\max,i} > 0\right)}{\sum_i A_i} \tag{5}$$

where A_i represents the area of subset i in the DIC measurement, $\varepsilon_{\max,i}$ represents the maximum principal strain of the subset i.

$$D_{\tilde{\varepsilon},m\&i} = \frac{\sum_i \left(\tilde{\varepsilon}_{i,m\&i} \cdot A_i \middle| \tilde{\varepsilon}_{i,m\&i} > K_0\right)}{\sum_i A_i} \tag{6}$$

where $\tilde{\varepsilon}_{i,m\&i}$ represents the equivalent strain of the mortar or interface subset i.

Fig. 10 shows the obtained $D_{\tilde{\varepsilon},m\&i}$ of the concrete slices with different coarse aggregate sizes under drying up to 60 days. The $D_{\tilde{\varepsilon},m\&i}$ of Concrete-S remained approximate 15 μm/m even dried for 60 days. In contrast, the $D_{\tilde{\varepsilon},m\&i}$ of Concrete-M and Concrete-L grew to 82 μm/m and 91 μm/m, respectively, indicating the relatively high microcracking risk in Concrete-M and Concrete-L.

Fig. 11 shows the drying-induced microcracks in the concrete slices with different coarse aggregate sizes (obtained using the lattice fracture model). In order to compare with the damage patterns identified using the DIC, only the microcracks with the width larger than 5 μm were displayed. As can be seen, two types of microcracks were obtained: (1) The microcracks (red) in the mortar phase showed radial patterns connecting coarse aggregates. (2) The microcracks (yellow) on the interface formed parallel to the surface of coarse aggregates. As shown in Fig. 12, the simulated microcrack patterns were in good correlation with the damage patterns identified from DIC. To quantify the relationship between the simulated microcrack patterns and the measured damage patterns, the damage index was plotted versus the area of >5 μm microcracks as shown in Fig. 13. As can be seen, the area of >5 μm

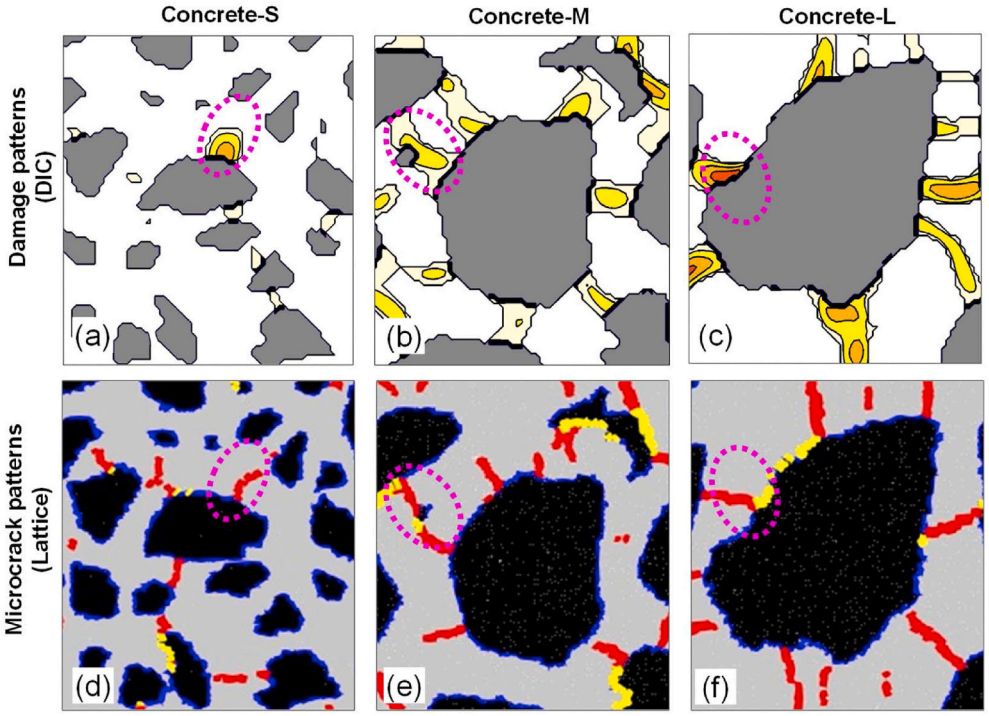

Fig. 12. Comparison between damage and microcrack patterns (>5 μm) in concrete slices with different coarse aggregate sizes under drying for 60 days.

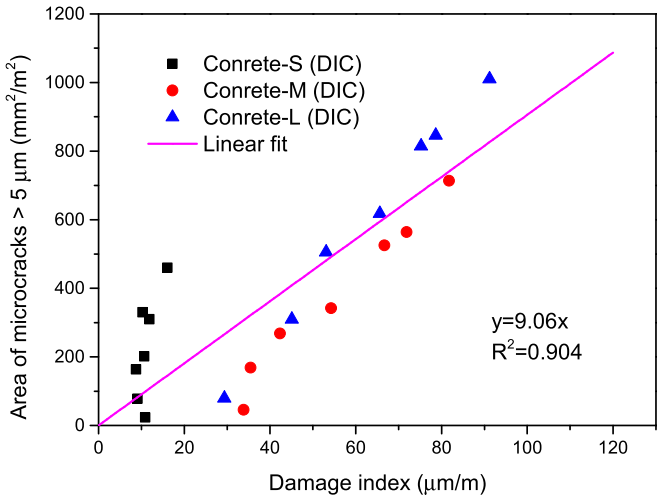

Fig. 13. Damage index *versus* area of >5 μm microcracks in concrete slices with different coarse aggregate sizes.

microcracks increases linearly with the increase of the damage index, illustrating that the damage index can be used to reflect the level of microcracking. For example, if the damage index is smaller than 20 μm/m, the microcracking risk of concrete will be low.

4.3. *Effect of aggregate size on microcracking in concrete*

As illustrated in sections 4.1 and 4.2, the drying-induced displacements and microcracking in concrete obtained using the lattice fracture model compared well with the DIC observations. This illustrates that the lattice fracture modelling was reliable for evaluating the effect of aggregate size on the drying-induced microcracking in concrete. In this section, the characteristics of the drying-induced microcracks, which were from the lattice fracture modelling, were discussed as follows.

As shown in Table 5, the coarse aggregate size significantly influenced the area of the microcracks >5 μm in width. For example, at 60 days since drying, the area of >5 μm microcracks in Concrete-S was 340.2 mm^2/m^2, while that of >5 μm microcracks in Concrete-M and Concrete-L increased to 582.7 mm^2/m^2 and 796.6 mm^2/m^2, respectively. This trend was in line with both the DIC observations (see Fig. 9) and the experimental observations (fluorescent epoxy impregnation) from literature [5,6]. However, the coarse aggregate size did not have strong impact on the microcracks' total area. For example, the

Table 5
Area of microcracks in concrete slices with different coarse aggregate sizes (mm^2/m^2).

Time since drying (days)	Area of microcracks (mm^2/m^2)					
	Concrete-S		Concrete-M		Concrete-L	
	>5 μm microcracks	Total microcracks	>5 μm microcracks	Total microcracks	>5 μm microcracks	Total microcracks
1	6.4	190.3	30.0	281.9	71.3	342.4
3	48.9	459.1	118.9	563.9	230.6	616.7
7	110.4	654.8	225.5	746.7	375.6	806.2
11	141.7	743.9	291.8	835.9	443.1	891.4
21	233.3	931.9	433.9	1009.6	622.2	1098.7
28	245.2	949.9	455.6	1035.5	643.8	1123.5
60	340.2	1106.3	582.7	1183.6	796.6	1281.2

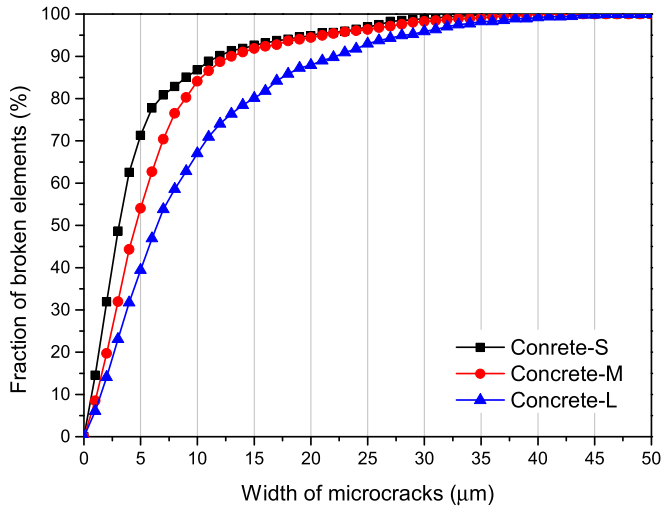

Fig. 14. Cumulative distribution of microcracks in concretes with different aggregate sizes under drying for 60 days.

microcracks' total areas were around 1200 mm^2/m^2 at 60 days since drying. Idiart et al. [8,9] also found that the simulated drying-induced microcrack patterns were not consistent with the experimental observations if the thin microcracks were considered in the comparison, because the microcracks smaller than 1 μm were difficult to be determined in experiments such as the fluorescent epoxy impregnation. In the numerical study of Grassl et al. [7], the microcracks' total area was even found to decrease as increasing the aggregate size. The current study also found that the number of small microcracks decreased with increasing the aggregate size (see Fig. 14). Hence, the statement that "the aggregate size increases the area of drying-induced microcracks" should be considered carefully.

4.4. Effect of aggregate size on tensile stress in concrete

According to the studies of Goltermann [10,11] and Moon [12], tensile stress shell will form tangentially to the aggregate due to the restraint of aggregate on the drying shrinkage of matrix, which could cause the formation and propagation of microcracks. However, there remains a gap in establishing the relationship among aggregate size, tensile stress shell, and drying-induced microcracks, because the value of the tensile stress was found to be independent of the aggregate size [10–12]. In this section, the patterns and thickness of tensile stress shell were obtained using the lattice fracture model, and used for analysing the effect of aggregate size on the microcracking in concrete.

Fig. 15 displays the distribution of coarse aggregates (black), the patterns of tensile stresses (larger than 1 MPa, blue), and the patterns of all microcracks (orange). As can be seen in Fig. 15a, c and e, tensile stress shells could form surrounding the coarse aggregates at the beginning of drying. With increasing the coarse aggregate size, the areas of tensile stress shells increased. At 60 days since drying (see Fig. 15b, d and f), the patterns of tensile stress shells were dispersed owing to the formation of microcracks.

Fig. 16 displays the patterns of the residual tensile stresses (>1 MPa) at the beginning of drying and the patterns of the microcracks (>5 μm) at 60 days since drying (Concrete-L). Two tensile stress shells were zoomed in Fig. 16b and c. Obviously, the large aggregate showed a larger tensile stress shell, which could increase the area of large microcracks (Fig. 16c). In addition, large microcracks seems to occur in the overlap area of two particles' tensile stress shells.

To directly clarify the influence of aggregate size on the tensile stress shell, the thickness of tensile stress shell in concrete was quantified as follows. At first, the total area ($A_{tot,agg}$) and total number (N_{agg}) of coarse aggregates in the DIC images were obtained using the digital image process (see Appendix B). By assuming coarse aggregates as spherical, the average diameter of coarse aggregates ($D_{ave,agg}$) was calculated as $\sqrt{4A_{tot,agg}/(\pi N_{agg})}$. The total area of tensile stress shell ($A_{tot,shell}$) was obtained from the lattice fracture modelling. Lastly, the average thickness of tensile stress shell ($\delta_{ave,shell}$) was calculated according to Eq. (7). Notably, the minimum stress (σ_{min}) in tensile stress shell exhibited in Figs. 15 and 16 was 1 MPa. However, the thickness of tensile stress shell would be different if the σ_{min} in tensile stress shell was different.

$$\delta_{ave,shell} = \left(\sqrt{\frac{4\left(A_{tot,agg} + A_{tot,shell}\right)}{\pi N_{agg}}} - D_{ave,agg} \right) \Big/ 2 \tag{7}$$

By using the data in Appendix B, the $\delta_{ave,shell}$ was calculated and exhibited in Fig. 17. The $\delta_{ave,shell}$ seems to increase linearly with the average diameter of coarse aggregates ($D_{ave,agg}$). For the tensile stress shell with a σ_{min} of 0.0 MPa, the $\delta_{ave,shell}$ increased from 1.09 mm to 2.13 mm as increasing the $D_{ave,agg}$ from 4.46 mm to 10.90 mm. Further, the $\delta_{ave,shell}$ decreased as the σ_{min} in tensile stress shell increased. For example, the $\delta_{ave,shell}$ decreased from 2.13 mm to 0.22 mm as the σ_{min} in the tensile stress shell increased from 0.0 MPa to 1.6 MPa in Concrete-L.

Based on the above analysis, the tensile stress shell thickness of coarse aggregates decreases with decreasing the coarse aggregate size, which will decrease the area of large microcracks. However, this raises a question: how the concrete with small coarse aggregates releases the drying shrinkage force in the mortar phase. By comparing Fig. 15b and f, the microcracks in Concrete-S seem to be dispersed by the coarse aggregates. Table 6 shows the numbers of ≤5 μm and >5 μm microcracks (broken elements) in the concrete slices with different coarse aggregate sizes (obtained using the lattice fracture model). As can be seen, the number of ≤5 μm microcracks in Concrete-S was much larger than that in Concrete-M and Concrete-L, while the number of >5 microcrack in Concrete-S was relatively small. For example, the number of ≤5 μm microcracks at 60 days since drying in Concrete-S was 27.53×10^3, which was much bigger than that in Concrete-M (18.08×10^3) and Concrete-L (14.15×10^3). For the concrete with constant coarse aggregate volume, the number of coarse aggregates will increase as decreasing the coarse aggregate size. Hence, more ITZ and connections between coarse aggregates will be introduced in the concrete, thereby increasing the propagation paths of small microcracks. Accordingly, the drying shrinkage force from the mortar phase can be released due to the formation of small microcracks.

To sum up, the coarse aggregate size shows two effects on the drying-induced microcracking in concrete: (1) The propagation paths of microcracks are increased as the coarse aggregate size decreases, which increases the number of small microcracks and releases the drying shrinkage force from mortar phase. (2) The thickness of tensile stress shell is decreased with decreasing the coarse aggregate size, which reduces the number of large microcracks. Hence, the area of large microcracks, which are more harmful for the mechanical and transport properties of concrete, can be reduced by decreasing the coarse aggregate size.

4.5. Practical importance and further work

(1) Practical importance

By combining the DIC and the lattice fracture modelling, the present study quantified the drying-induced non-uniform stresses/strains of the concrete slices with different coarse aggregate sizes. This provides a better understanding of the effect of coarse aggregate size on the drying-induced microcracking in concrete. Further, as illustrated in Fig. 16, the two aggregates' tensile stress shells could have overlap. This overlap seems to cause large microcracks in concrete. A hypothesis was proposed that the large drying-induced microcracks in concrete can be reduced by controlling the area of tensile stress shells' overlap, which might be

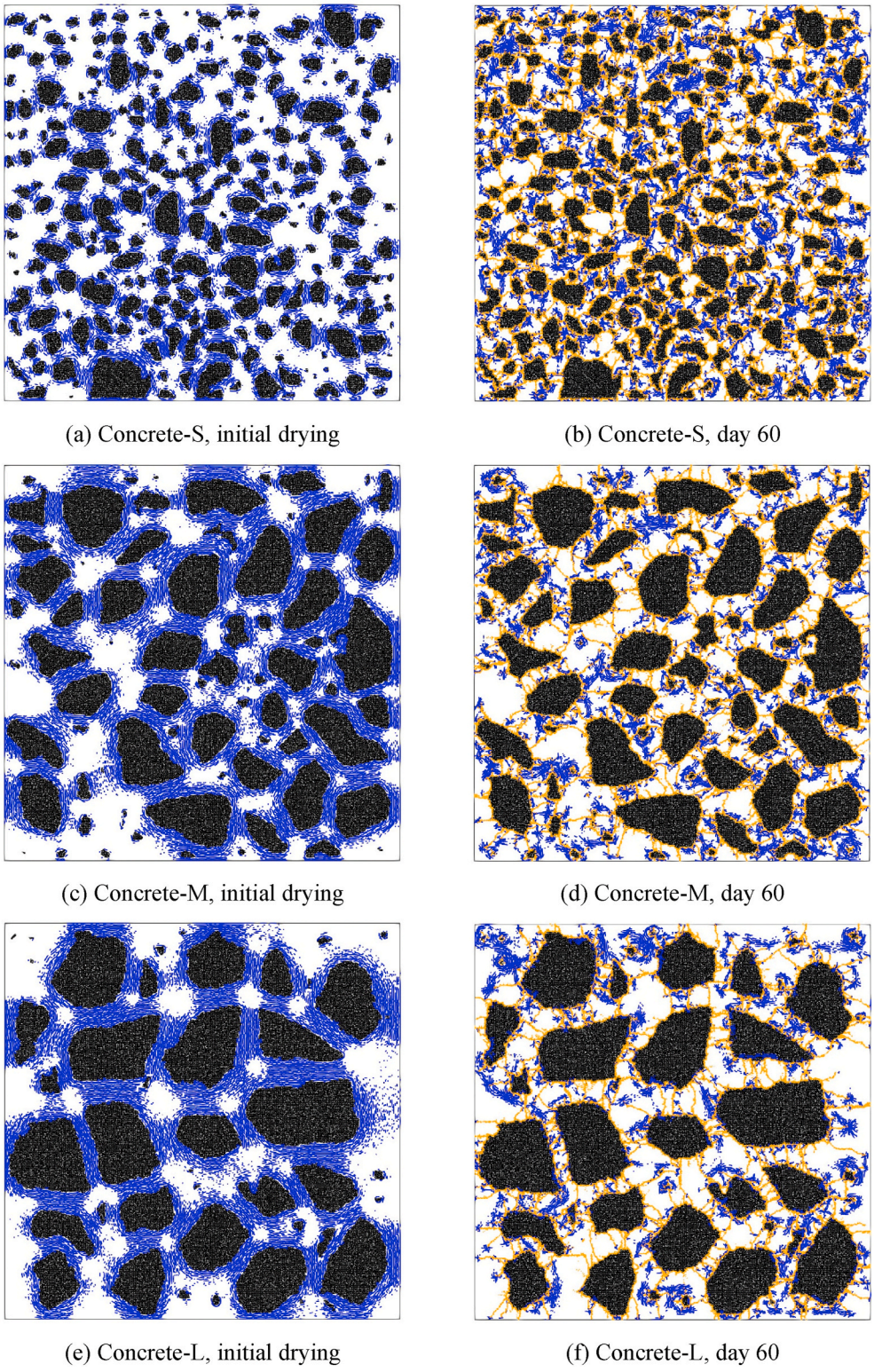

(a) Concrete-S, initial drying (b) Concrete-S, day 60

(c) Concrete-M, initial drying (d) Concrete-M, day 60

(e) Concrete-L, initial drying (f) Concrete-L, day 60

Fig. 15. Patterns of tensile stresses (>1 MPa) in concrete slices with different aggregate sizes at the beginning of drying (left) and 60 days since drying (right). Note: black, blue and orange represent coarse aggregates, tensile stresses >1 MPa, and total microcracks, respectively. Drying-induced force imposed on mortar elements were 0.30×10^{-3} kN in left figures and 4.4×10^{-3} kN in right figures. (For interpretation of the references to colour in this figure legend, the reader is referred to the Web version of this article.)

helpful for concrete mix design. For example, as shown in Fig. 17, the tensile stress shells' thickness was proportional to the coarse aggregate size. For $\sigma_{\min} = 0$ MPa, $\delta_{ave,shell} = 0.203 D_{ave,agg}$. By using the data shown in Fig. 17, the concrete with the $D_{ave,agg}$ of 10.9 mm (volume fraction = 0.4) showed the tensile stress shells' overlap (see Fig. 18a). Based on the linear relationship between $\delta_{ave,shell}$ and $D_{ave,agg}$, the tensile stress shells' thickness for the $D_{ave,agg}$ of 4.45 mm was calculated as 0.90 mm. As shown in Fig. 18b, below this size the concrete will not show the tensile stress shells' overlap if the coarse aggregates are homogenously distributed (coarse aggregates' volume fraction = 0.4). It is noted that this calculation was in two-dimension. Because $D_{ave,agg}$ was calculated from the cross-section image of coarse aggregates, $D_{ave,agg}$ was smaller than the coarse aggregates' size, In the three-dimensional calculation, the relationship between the real coarse aggregate size and the tensile stress shells' thickness should be considered.

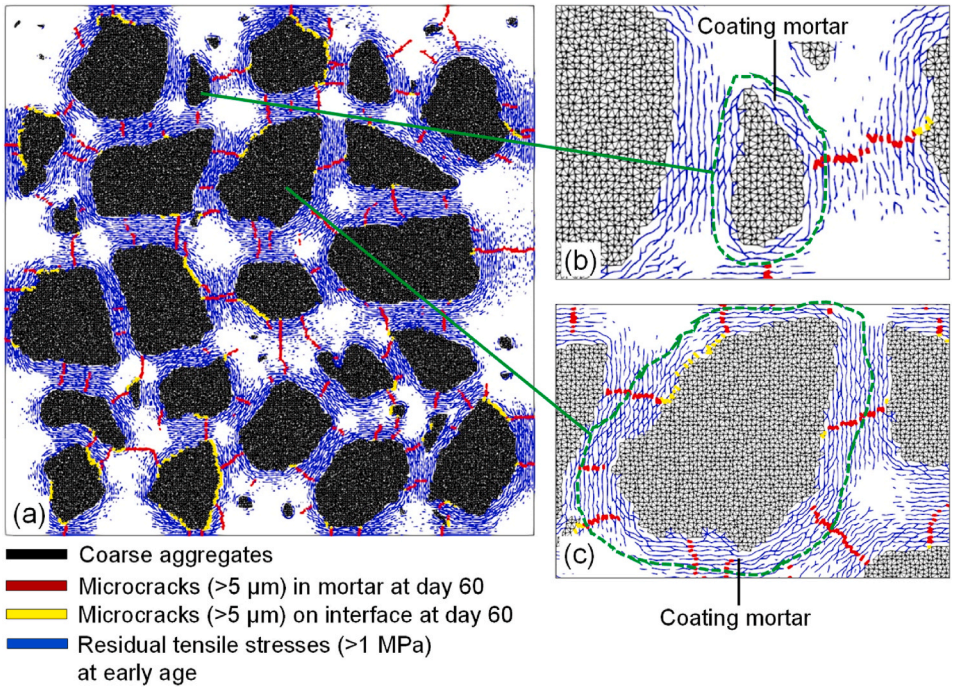

Fig. 16. Patterns of tensile stresses (>1 MPa) at the beginning of drying and microcracks (>5 μm) at day 60 since drying in Concrete-L.

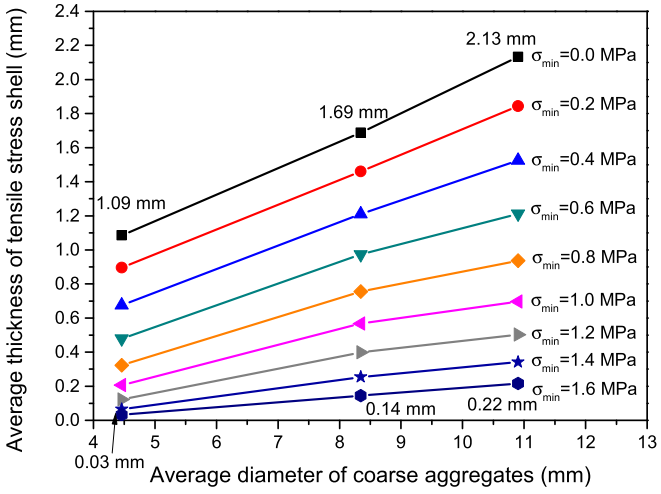

Fig. 17. Average thickness of tensile stress shell *versus* average diameter of coarse aggregates (at the beginning of drying).

(2) Further work

Since the ITZ normally shows poor mechanical properties, the influence of the ITZ on the drying-induced microcracking in concrete should also be discussed. One the one hand, more ITZ will be introduced in concrete if small aggregates are used. As indicated by Goltermann [10,11], shear stresses could rise along the ITZ and cause shear cracks. However, owing to the compressive stresses around the ITZ, the width of the microcracks along the ITZ is much smaller than that of the radial microcracks in the matrix. Moreover, the ITZ's porosity will be reduced as the aggregate size decreases [52]. The above two mechanisms can be used to explain the better transport properties of the concrete (after drying) that contains small aggregates [53]. According to the microcrack patterns (obtained using the lattice fracture modelling) as shown in Fig. 11, the microcracks on the interface elements were also less significant than that in the mortar elements. Hence, more attention should be paid on the drying-induced microcracking in matrix. Nevertheless, the quantification of the aggregate size's impact on the porosity and mechanical properties of ITZ is an important research topic to investigate the drying-induced microcracking of concrete with different aggregate sizes in further work. In addition to causing the deterioration of mechanical properties, the microcracking might accelerate the mass transport and reduce the durability of concrete [46]. This is another research direction in further work.

Table 6
Number of microcracks in concrete slices with different coarse aggregate sizes.

Time since drying (days)	Number of microcracks					
	Concrete-S		Concrete-M		Concrete-L	
	≤5 μm microcracks	>5 μm microcracks	≤5 μm microcracks	>5 μm microcracks	≤5 μm microcracks	>5 μm microcracks
1	15720	20	11743	97	10147	233
3	21766	164	15393	387	12300	690
7	24189	331	16676	724	13092	1058
11	25115	415	17004	926	13415	1225
21	26553	697	17706	1344	13947	1643
28	26634	736	17795	1405	14002	1688
60	27534	1016	18076	1734	14151	1999

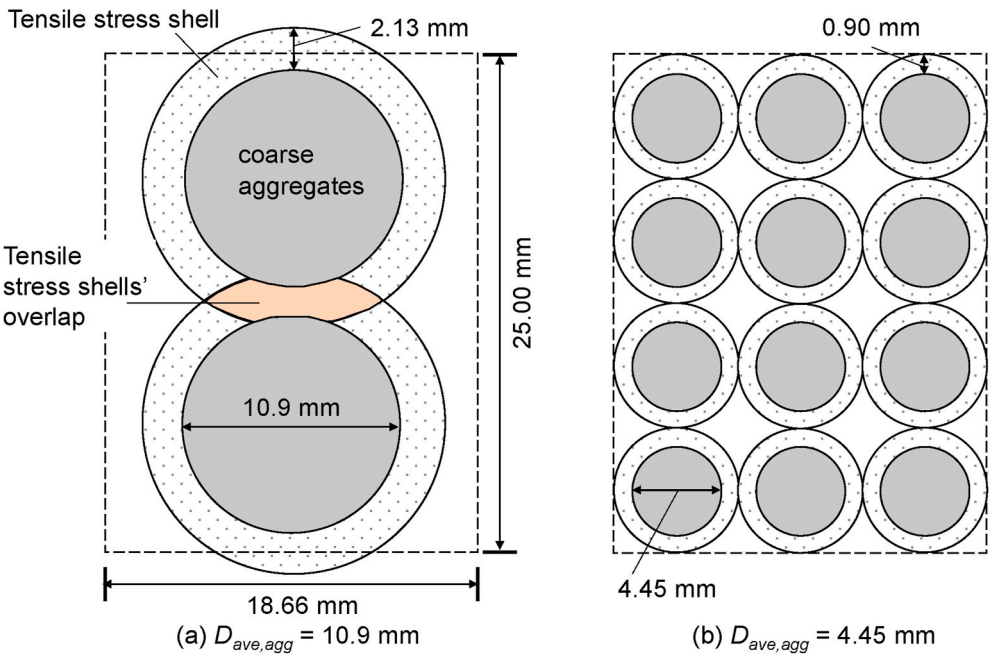

Fig. 18. Schematic diagram of reducing tensile stress shells' overlap between coarse aggregates by adjusting $D_{ave,agg}$ (coarse aggregates' volume fractions = 0.40).

Notably, the real concrete structures could suffer from other factors such as non-uniform drying, moisture gradients and differential shrinkage [35]. These factors could interact with the components of concrete. For example, the moisture diffusion in concrete is significantly influenced by the spatial distribution of aggregates [54]. Hence, the volume, size, shape of aggregates should be considered to analyse the influence of moisture gradients on the microcracking in concrete. Further work should therefore incorporate the interaction mechanisms of these factors to reveal the drying-induced microcracking behaviour of real concrete structures.

5. Conclusions

This study deals with the effect of coarse aggregate size on the non-uniform strains, residual stresses and microcracking of the concrete slices (thickness = 10 mm) with different coarse aggregate sizes (5–10 mm, 10–16 mm, 16–20 mm) dried at 20 °C, 40% RH up to 60 days by combining the DIC and the lattice fracture modelling. The coarse aggregates' volume fractions were 0.37, 0.41, and 0.42 in the concrete slices with 5–10 mm, 10–16 mm and 16–20 mm coarse aggregates, respectively. The following conclusions can be drawn:

(1) According to the DIC observations, the bulk drying shrinkage of concrete decreased with increasing the coarse aggregate size, while the local displacements became more non-uniform. The maximum (ε_{max}) and minimum (ε_{min}) principal strains determined using the DIC were used to identify damage patterns and damage index ($D_{\tilde{\varepsilon}}$) in concrete slices. With increasing the drying time to 60 days, the $D_{\tilde{\varepsilon}}$ of the concrete slice with 5–10 mm coarse aggregates remained approximate 15 μm/m, while the $D_{\tilde{\varepsilon}}$ of the concrete slices with 10–16 mm, and 16–20 mm coarse aggregates increased to 82 μm/m and 91 μm/m, respectively, illustrating the high cracking risk in the concrete with large coarse aggregate size.

(2) The drying-induced microcracking of concrete slices was simulated by imposing the drying-induced forces onto the mortar and interface elements. The simulated bulk drying shrinkage of concrete slice decreased as increasing the coarse aggregate size, which were in line with the DIC observations. The simulated patterns of the microcracks larger than 5 μm in width were consistent with the damage patterns captured using the DIC.

(3) The coarse aggregate size shows two effects on the drying-induced microcracking in concrete: 1) With decreasing the coarse aggregate size in the concretes, the propagation paths of microcracking are increased, which increases the number of microcracks and releases the drying shrinkage force from mortar phase. 2) The thickness of tensile stress shell is decreased with decreasing the coarse aggregate size, thereby decreasing the area of large microcracks. At the beginning of drying, the thickness of tensile stress shell decreased from 2.13 mm to 1.09 mm (minimum stress in tensile stress shell was 0.0 MPa) with decreasing the coarse aggregate size from 16-20 mm to 5–10 mm. At 60 days since drying, the area of the microcracks larger than 5 μm in width decreased from 796.6 mm^2/m^2 to 340.2 mm^2/m^2.

(4) The large microcracks are relevant to the overlap of the tensile stress shells between coarse aggregates. The quantification of the tensile stress shells' thickness is beneficial to reduce the tensile stress shells' overlap by controlling the coarse aggregate size, which might be helpful for concrete mix design from the view point of reducing large microcracks.

CRediT authorship contribution statement

Peng Gao: Visualization, Writing - original draft, Writing - review & editing. **Yang Chen**: Methodology. **Haoliang Huang**: Writing - review & editing. **Zhiwei Qian**: Software. **Erik Schlangen**: Software. **Jiangxiong Wei**: Conceptualization, Supervision, Writing - review & editing. **Qijun Yu**: Supervision.

Declaration of competing interest

The authors declare that they have no known competing financial interests or personal relationships that could have appeared to influence the work reported in this paper.

Acknowledgements

This work was supported by the National Key Research and

Development Program (2017YFB0310001-02), the National Natural Science Foundation of China (Grant No. 51672084, 51772103, 51872097, and 52002129), and the China Postdoctoral Science Foundation funded project (Grant No. 2019M650199).

Appendix A. Surface of concrete slice after cutting process

The speed of cutting machine should be adjusted according to the properties of concrete. In the present study, the cutting speed was set as 200 r/min to ensure that the surface was smooth and no significant cracks were observed. Fig. A1 shows a photo of concrete slice after the cutting process.

Fig. A.1. Photo of concrete slice after cutting process

Appendix B. Parameters for calculating average thickness of coarse aggregates' tensile stress shells

Table B.1 shows the obtained number (N_{agg}), average diameter ($D_{ave,agg}$), and total area ($A_{tot,agg}$) of coarse aggregates in the DIC images of Concrete-S, Concrete-M and Concrete-L, respectively. The obtained $D_{ave,agg}$ was smaller than the coarse aggregates' size, because $D_{ave,agg}$ was calculated from the cross-section image of coarse aggregates. Fig. B1 shows the total area of tensile stress shells ($A_{tot,\ stress}$) with different minimum stresses. As can be seen, as the σ_{min} in tensile stress shell was relatively higher (e.g. >1 MPa), the $A_{tot,\ stress}$ in Concrete-S was smaller than that in Concrete-M and Concrete-L. However, as the σ_{min} in tensile stress shell decreased to 0.0 MPa, the $A_{tot,\ stress}$ in Concrete-S became much larger than that in Concrete-M and Concrete-L. This illustrates that small aggregates play a role in dispersing tensile stress by increasing the total area of tensile stress shells.

Table B.1
Parameters of coarse aggregates in DIC images

	Number of coarse aggregates	Total area of coarse aggregates (mm^2)	Average diameter of coarse aggregates (mm)	Coarse aggregate size (mm)
Concrete-S	237	3700	4.46	5–10
Concrete-M	75	4100	8.34	10–16
Concrete-L	45	4200	10.90	16–20

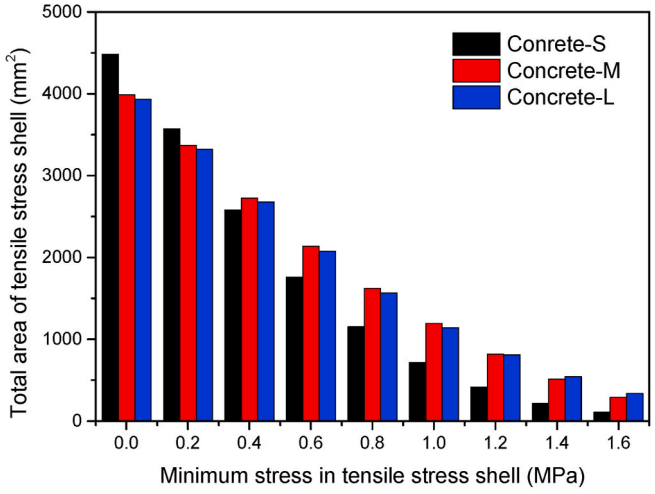

Fig. B.1. Total area of tensile stress shells with different minimum stresses (at beginning of drying).

References

[1] Bissonnette B, Pierre P, Pigeon M. Influence of key parameters on drying shrinkage of cementitious materials. Cement Concr Res 1999;29:1655–62.
[2] Chen PW, Chung DD. Low-drying-shrinkage concrete containing carbon fibers. Compos B Eng 1996:269–74.
[3] Afroughsabet V, Biolzi L, Monteiro PJM. The effect of steel and polypropylene fibers on the chloride diffusivity and drying shrinkage of high-strength concrete. Compos B Eng 2018;139:84–96.
[4] Qin R, Hao H, Rousakis T, Lau D. Effect of shrinkage reducing admixture on new-to-old concrete interface. Compos B Eng 2019:167346–55.
[5] Bisschop J, van Mier JGM. Effect of aggregates on drying shrinkage microcracking in cement-based composites. Mater Struct 2002;35:453–61.
[6] Wu Z, Wong HS, Buenfeld NR. Influence of drying-induced microcracking and related size effects on mass transport properties of concrete. Cement Concr Res 2015;68:35–48.
[7] Grassl P, Wong HS, Buenfeld NR. Influence of aggregate size and volume fraction on shrinkage induced micro-cracking of concrete and mortar. Cement Concr Res 2010;40:85–93.
[8] Idiart AE, López CM, Carol I. Modeling of drying shrinkage of concrete specimens at the meso-level. Mater Struct 2011;44:415–35.
[9] Idiart A, Bisschop J, Caballero A, Lura P. A numerical and experimental study of aggregate-induced shrinkage cracking in cementitious composites. Cement Concr Res 2012;42:272–81.
[10] Goltermann P. Mechanical predictions on concrete deterioration. Part 1: eigenstresses in concrete. ACI Mater J 1994;91:543–50.
[11] Goltermann P. Mechanical predictions of concrete deterioration. Part 2: classification of crack patterns. ACI Mater J 1995;92:58–63.
[12] Moon JH. Shrinkage, residual stress, and cracking in heterogeneous materials. West Lafayette, Indiana: Purdue University; May 2006. PhD thesis.
[13] Neubauer CM, Jennings HM. The use of digital images to determine deformation throughout a microstructure Part I Deformation mapping technique. J Mater Sci 2000;35:5741–9.
[14] Peters WH, Ranson WF, Sutton MA, Chu TC, Anderson J. Application of digital correlation methods to rigid body mechanics. Opt Eng 1983;22:38–42.
[15] Helfrick MN, Niezrecki C, Avitabile P, Schmidt T. 3D digital image correlation methods for full-field vibration measurement. Mech Syst Signal Process R 2011;25:917–27.
[16] Pan B, Xie HM, Yang L, Wang ZY. Accurate measurement of satellite antenna surface using 3D digital image correlation technique. Strain 2009;45:194–200.
[17] Tajmir-Riahi A, Moshiri N, Mostofinejad D. Inquiry into bond behavior of CFRP sheets to concrete exposed to elevated temperatures – experimental & analytical evaluation. Compos B Eng 2019;173:106897.
[18] Moelich GM, Kruger J, Combrinck R. Plastic shrinkage cracking in 3D printed concrete. Compos B Eng 2020;200:108313.
[19] Nguyen H, Kinnunen P, Carvelli V, Mastali M, Illikainen M. Strain hardening polypropylene fiber reinforced composite from hydrated ladle slag and gypsum. Compos B Eng 2019;158:328–38.
[20] Teramoto A, Watanabe M, Murakami R, Ohkubo T. Visualization of internal crack growth due to alkali–silica reaction using digital image correlation. Construct Build Mater 2018;190:851–60.
[21] Dzaye ED, Tsangouri E, Spiessens K, Schutter GD, Aggelis DG. Digital image correlation (DIC) on fresh cement mortar to quantify settlement and shrinkage. Arch Civ Mech Eng 2019;19:205–14.
[22] Huang Z, Tu Y, Meng S, Sabau C, Popescu C, Sas G. Experimental study on shear deformation of reinforced concrete beams using digital image correlation. Eng Struct 2019;181:670–98.
[23] Bertelsen IMG, Kragh C, Cardinaud G, Ottosen LM, Fischer G. Quantification of plastic shrinkage cracking in mortars using digital image correlation. Cement Concr Res 2019;123:105761.
[24] Niu Y, Huang H, Zhang J, Jin W, Wei J, Yu Q. Development of the strain field along the crack in ultra-high-performance fiber-reinforced concrete (UHPFRC) under bending by digital image correlation technique. Cement Concr Res 2019;125:105821.
[25] Moelich GM, Kruger J, Combrinck R. Plastic shrinkage cracking in 3D printed concrete. Compos B Eng 2020;200:108313.
[26] Lagier F, Jourdain X, Sa CD, Benboudjema F, Colliat JB. Numerical strategies for prediction of drying cracks in heterogeneous materials: comparison upon experimental results. Eng Struct 2011;33:920–31.
[27] Mauroux T, Benboudjema F, Turcry P, Aït-Mokhtar A, Deves O. Study of cracking due to drying in coating mortars by digital image correlation. Cement Concr Res 2012;42:1014–23.
[28] Maruyama I, Sasano H. Strain and crack distribution in concrete during drying. Mater Struct 2014;47:517–32.
[29] Maruyama I, Sugie A. Numerical study on drying shrinkage of concrete affected by aggregate size. J Adv Concr Technol 2014;12:279–88.
[30] Maruyama I, Sasano H, Lin M. Impact of aggregate properties on the development of shrinkage-induced cracking in concrete under restraint conditions. Cement Concr Res 2016;85:82–101.
[31] Chen Y, Wei J, Huang H, Jin W, Yu Q. Application of 3D-DIC to characterize the effect of aggregate size and volume on non-uniform shrinkage strain distribution in concrete. Cement Concr Compos 2018;86:178–89.
[32] Schlangen E, Koenders EAB, Breugel VK. Influence of internal dilation on the fracture behaviour of multi-phase materials. Eng Fract Mech 2007;74:18–33.
[33] Gao P, Chen Y, Huang H, Qian Z, Schlangen E, Wei J, Yu Q. Investigation of drying-induced non-uniform deformation, stress, and micro-crack propagation in concrete. Cement Concr Compos 2020;114:103786.
[34] Gao P, Chen Y, Huang H, Qian Z, Schlangen E, Wei J, Yu Q. Effect of relative humidity on drying-induced damage in concrete: a comparative study of digital image correlation and lattice modelling. Mater Des 2020;196:109128.
[35] Samouh H, Rozière E, Loukili A. The differential drying shrinkage effect on the concrete surface damage: experimental and numerical study. Cement Concr Res 2017;102:212–24.
[36] GB T50081-2002, Standard for test method of mechanical properties on ordinary concrete. China: China Academy of Building Research; 2002.
[37] Berton S, Bolander JE. Crack band model of fracture in irregular lattices. Comput Methods Appl Mech Eng 2006;195:7272. 7182.
[38] Qian Z, Schlangen E, Ye G, Breugel KV. Prediction of mechanical properties of cement paste at microscale. Mater Construcción 2010;60:7–18.
[39] Qian Z. Multiscale modelling of fracture processes in cementitious materials. Delft, The Netherlands: Dissertation, Delft University of Technology; 2012.
[40] Qian Z, Schlangen E, Ye G, Van Breugel K. Modeling framework for fracture in multiscale cement-based material structures. Materials 2017;10:587.
[41] Luković M, Šavija B, Schlangen E, Ye G, Breugel KV. A 3D lattice modelling study of drying shrinkage damage in concrete repair systems. Materials 2016;9:575.
[42] Liu L, Wang X, Chen H, Wan C, Zhang M. Numerical modeling of drying shrinkage deformation of cement-based composites by coupling multiscale structure model with 3D lattice analyses. Comput Struct 2017;178:88–104.

[43] Liu L, Wang X, Chen H, Wan C. Microstructure-based modelling of drying shrinkage and microcracking of cement paste at high relative humidity. Construct Build Mater 2016;126:410–25.
[44] Zhang H, Šavija B, Figueiredo SC, Schlangen E. Experimentally validated multi-scale modelling scheme of deformation and fracture of cement paste. Cement Concr Res 2017;102:175–86.
[45] Zhang H, Xu Y, Gan Y, Chang Z, Schlangen E, Šavija B. Combined experimental and numerical study of uniaxial compression failure of hardened cement paste at micrometre length scale. Cement Concr Res 2019;126:105925.
[46] Šavija B, Pacheco J, Schlangen E. Lattice modeling of chloride diffusion in sound and cracked concrete. Cement Concr Compos 2013;42:30–40.
[47] Diamond S, Huang J. The ITZ in Concrete – a different view based on image analysis and SEM observations. Cement Concr Compos 2001;23:179–88.
[48] Grasley ZC, Leung CK. Desiccation shrinkage of cementitious materials as an aging, poroviscoelastic response. Cement Concr Res 2011;41:77–89.
[49] Bažant ZP, Jirásek M. Creep and hygrothermal effects in concrete structures. Dordrech, The Netherlands: Springer; 2018.
[50] Grasley ZC, Lange DA, Ambrosia MDD. Internal relative humidity and drying stress gradients in concrete. Mater Struct 2006;390:901–9.
[51] Mazars J. A description of micro- and macroscale damage of concrete structures. Eng Fract Mech 1986;25:729–37.
[52] Elsharief A, Cohen MD, Olek J. Influence of aggregate size, water cement ratio and age on the microstructure of the interfacial transition zone. Cement Concr Res 2003;33:1837–49.
[53] Wong HS, Zobel M, Buenfeld NR, Zimmerman RW. Influence of the interfacial transition zone and microcracking on the diffusivity, permeability and sorptivity of cement-based materials after drying. Mag Concr Res 2009;61:571–89.
[54] Mu R, Tian W, Guo Y. Effect of aggregate on drying shrinkage of concrete. Adv Mater Res 2010;168–170:701–8.